The Astrophysical Journal, 740:63 (10pp), 2011 October 20 doi:10.1088/0004-637X/740/2/63

GAS AND DUST IN A SUBMILLIMETER GALAXY AT $z = 4.24$ FROM THE *HERSCHEL* ATLAS

P. Cox[1], M. Krips[1], R. Neri[1], A. Omont[2], R. Güsten[3], K. M. Menten[3], F. Wyrowski[3], A. Weiß[3], A. Beelen[4], M. A. Gurwell[5], H. Dannerbauer[6], R. J. Ivison[7,8], M. Negrello[9], I. Aretxaga[10], D. H. Hughes[10], R. Auld[11], M. Baes[12], R. Blundell[5], S. Buttiglione[13], A. Cava[14], A. Cooray[15], A. Dariush[11,16], L. Dunne[17], S. Dye[17], S. A. Eales[11], D. Frayer[18], J. Fritz[12], R. Gavazzi[2], R. Hopwood[9], E. Ibar[7], M. Jarvis[13], S. Maddox[17], M. Michałowski[8], E. Pascale[11], M. Pohlen[11], E. Rigby[17], D. J. B. Smith[17], A. M. Swinbank[19], P. Temi[20], I. Valtchanov[21], P. van der Werf[22], and G. de Zotti[13]
[1] IRAM, 300 rue de la piscine, F-38406 Saint-Martin d'Hères, France; cox@iram.fr
[2] Institut d'Astrophysique de Paris, Université Pierre et Marie Curie and CNRS (UMR7095), 98 bis boulevard Arago, 75014 Paris, France
[3] MPIfR, Auf dem Hügel 69, 53121 Bonn, Germany
[4] IAS, Bât. 121, Université Paris-Sud, F-91405 Orsay Cedex, France
[5] Harvard-Smithsonian Center for Astrophysics, 60 Garden Street, Mail Stop 42, Cambridge, MA 02138, USA
[6] AIM, CEA/DSM-CNRS-Université de Paris Diderot, DAPNIA/Service d'Astrophysique, CEA Saclay, Orme des Merisiers, 91191 Gif-sur-Yvette, France
[7] UK Astronomy Technology Centre, Royal Observatory, Blackford Hill, Edinburgh EH9 3HJ, UK
[8] Scottish Universities Physics Alliance, Institute for Astronomy, University of Edinburgh, Royal Observatory, Blackford Hill, Edinburgh EH9 3HJ, UK
[9] Department of Physics and Astronomy, The Open University, Milton Keynes MK7 6AA, UK
[10] Instituto Nacional de Astrofísica, Optica y Electrónica, Aptdo. Postal 51 y 216, 72000 Puebla, Mexico
[11] School of Physics and Astronomy, Cardiff University, The Parade, Cardiff CF24 3AA, UK
[12] Sterrenkundig Observatorium, Universiteit Gent, Krijgslaan 281, S9, B-9000 Gent, Belgium
[13] INAF-Osservatorio Astronomico di Padova, Vicolo dell'Osservatorio 5, I-35122 Padova, Italy & SISSA, Via Bonomea 265, I-34136 Trieste, Italy
[14] Departamento de Astrofísica, Facultad de CC. Físicas, Universidad Complutense de Madrid, E-28040 Madrid, Spain
[15] Department of Physics and Astronomy, University of California, Irvine, CA 92697, USA
[16] School of Astronomy, Institute for Research in Fundamental Sciences (IPM), P.O. Box 19395-5746, Tehran, Iran
[17] School of Physics and Astronomy, University of Nottingham, University Park, Nottingham NG7 2RD, UK
[18] National Radio Astronomy Observatory, P.O. Box 2, Green Bank, WV 24944, USA
[19] Institute for Computational Cosmology, Durham University, South Road, Durham DH1 3EE, UK
[20] Astrophysics Branch, NASA Ames Research Center, Mail Stop 245-6, Moffett Field, CA 94035, USA
[21] Herschel Science Center, ESAC, ESA, P.O. Box 78, 28691 Villanueva de la Cañada, Madrid, Spain
[22] Leiden Observatory, Leiden University, P.O. Box 9513, 2300 RA Leiden, The Netherlands
Received 2011 March 1; accepted 2011 July 15; published 2011 September 30

ABSTRACT

We report ground-based follow-up observations of the exceptional source, ID 141, one of the brightest sources detected so far in the *Herschel* Astrophysical Terahertz Large Area Survey cosmological survey. ID 141 was observed using the IRAM 30 m telescope and Plateau de Bure interferometer (PdBI), the Submillimeter Array, and the Atacama Pathfinder Experiment submillimeter telescope to measure the dust continuum and emission lines of the main isotope of carbon monoxide and carbon ([C I] and [C II]). The detection of strong CO emission lines with the PdBI confirms that ID 141 is at high redshift ($z = 4.243 \pm 0.001$). The strength of the continuum and emission lines suggests that ID 141 is gravitationally lensed. The width ($\Delta V_{\rm FWHM} \sim 800\,{\rm km\,s^{-1}}$) and asymmetric profiles of the CO and carbon lines indicate orbital motion in a disk or a merger. The properties derived for ID 141 are compatible with an ultraluminous ($L_{\rm FIR} \sim (8.5 \pm 0.3) \times 10^{13}\,\mu_{\rm L}^{-1}\,L_{\odot}$, where $\mu_{\rm L}$ is the amplification factor), dense ($n \approx 10^4\,{\rm cm^{-3}}$), and warm ($T_{\rm kin} \approx 40\,{\rm K}$) starburst galaxy, with an estimated star formation rate of (0.7–1.7) $\times 10^4\,\mu_{\rm L}^{-1}\,M_{\odot}\,{\rm yr^{-1}}$. The carbon emission lines indicate a dense ($n \approx 10^4\,{\rm cm^{-3}}$) photon-dominated region, illuminated by a far-UV radiation field a few thousand times more intense than that in our Galaxy. In conclusion, the physical properties of the high-z galaxy ID 141 are remarkably similar to those of local ultraluminous infrared galaxies.

Key words: galaxies: active – galaxies: evolution – galaxies: high-redshift – galaxies: individual (ID 141) – galaxies: starburst – submillimeter: galaxies

Online-only material: color figures

1. INTRODUCTION

Over the last decade, submillimeter surveys have revolutionized our understanding of the formation and evolution of galaxies by uncovering a population of high-redshift, dust-obscured systems that are forming stars at a tremendous rate (e.g., Smail et al. 1997; Hughes et al. 1998; Blain et al. 2002). Submillimeter galaxies (SMGs) are high-redshift analogs of the local ultraluminous infrared galaxies (ULIRGs) in terms of their CO, radio, and infrared properties (Tacconi et al. 2008, 2010). The general importance of ultraluminous sources for galaxy evolution has been highlighted by recent *Spitzer* and *Herschel* results that show that these sources contribute significantly to the total amount of star formation in the early universe (Magnelli et al. 2009).

Until recently, observations at submillimeter wavelengths have been conducted mainly from the ground and/or from balloon experiments and covered only relatively small areas of the sky. The discovery rate of rare objects such as strongly lensed sources was therefore limited. Nevertheless, due to selection effects, many of the known high-redshift submillimeter sources are gravitationally lensed, such as IRAS 10214+4724, which is amplified by a factor of ∼10 (Rowan-Robinson et al. 1991; Downes et al. 1995). However, these limited surveys found few

Table 1
Photometric Measurements of ID 141

Wavelength (μm)	Flux Density (mJy)	Facility
250	115 ± 19	SPIRE[a]
350	192 ± 30	SPIRE[a]
500	204 ± 32	SPIRE[a]
870	102 ± 8.8	LABOCA[b]
880	90 ± 5	SMA
1200	36 ± 2	MAMBO-2[c]
1950	9.7 ± 0.9	PdBI
2750	1.8 ± 0.3	PdBI
3000	1.6 ± 0.2	PdBI
3290	1.2 ± 0.1	PdBI

Notes.
[a] *Herschel*.
[b] APEX.
[c] 30 m.

strongly lensed sources. This situation changed dramatically with the 87 deg^2 deep field survey at wavelengths of 1.4 and 2.0 mm taken with the South Pole Telescope (Vieira et al. 2010) and, since then, the *Herschel Space Observatory* (Pilbratt et al. 2010) has been able to map an enormously extended area of the sky at submillimeter wavelengths. In particular, the wide-area *Herschel* Astrophysical Terahertz Large Area Survey or H-ATLAS (Eales et al. 2010) with the Spectral and Photometric Imaging Receiver or SPIRE (Griffin et al. 2010) and the Photodetector Array Camera and Spectrometer or PACS (Poglitsch et al. 2010) instruments will ultimately map a total of about 570 deg^2 to around (or below) the confusion limit in five bands from 100 to 500 μm. In addition to uncovering hundreds of thousands of SMGs, the *Herschel* surveys will enable discovery of the brightest infrared sources in the universe, including many strongly lensed sources because of the high magnification bias in the submillimeter bands (Blain 1996). These surveys and samples of lensed sources are unique and will remain so for the foreseeable future.

Negrello et al. (2007) predicted that most of the 500 μm brightest sources (i.e., with $S_{500\,\mu\mathrm{m}} > 100$ mJy) detected at high redshift by the *Herschel Space Observatory* will consist of strongly lensed SMGs, a population of local star-forming galaxies—easily identified in shallow Sloan Digital Sky Survey (SDSS) images—a relatively small fraction of radio-bright active galactic nuclei (AGNs)—easily identifiable in shallow radio surveys (Negrello et al. 2010)—as well as nearby spirals. The ongoing surveys have confirmed this prediction with the detection of submillimeter-bright ($S_{500\,\mu\mathrm{m}} > 100$ mJy) sources that have been shown, based on ground-based follow-up observations, to be gravitationally lensed SMGs in the distant ($z \sim 1.5$–4) universe (Negrello et al. 2010; Conley et al. 2011). The lensing boosts the sensitivity of observations and improves their spatial resolution enabling detailed studies of the populations responsible for the bulk of the background (Blain et al. 1999; Hopwood et al. 2010). Follow-up observations with ground-based telescopes, especially by (sub)millimeter facilities are essential to further probe the physical characteristics of these outstanding sources. A recent and striking example of a lensed source discovered in the pre-*Herschel* era in the submillimeter is the $z = 2.3$ galaxy SMM J1235−0102 (Swinbank et al. 2010) or the "Eyelash." This typical SMG, which is amplified by a factor of $\sim$35×, has been observed in exquisite detail, enabling diagnosis of the properties of its molecular and atomic gas (Danielson et al. 2011).

Here, we report ground-based follow-up observations of an exceptional source uncovered by the H-ATLAS survey, HATLASJ142413.9+022304 (hereafter ID 141), including a measurement of its redshift and a derivation of the properties of its molecular and atomic gas content.

Throughout the paper, we use a ΛCDM cosmology with $H_0 = 71\,\mathrm{km\,s^{-1}\,Mpc^{-1}}$, $\Omega_m = 0.27$, and $\Omega_\Lambda = 1-\Omega_m$ (Spergel et al. 2003).

2. OBSERVATIONS AND RESULTS

The source ID 141 is one of the brightest sources detected so far in the *Herschel* deep surveys. It is the strongest source peaking at 500 μm in the 100 deg^2 currently surveyed in the H-ATLAS program and yet found in the *Herschel* cosmological surveys. The source position as determined by *Herschel* is R.A. 14:24:13.9 decl. +02:23:04 (J2000.0) and is located in the so-called GAMA 15 h field. Its flux densities, as measured with SPIRE, are in excess of 100 mJy in all bands with a spectral energy distribution (SED) still rising from 250 to 500 μm (Table 1), indicating that the redshift of this exceptional source must be high ($z > 3$).

Imaging from the SDSS (DR7; York et al. 2000) reveals a faint optical counterpart with the following magnitudes: $u = 23.45 \pm 1.33$, $g = 22.99 \pm 0.35$, $r = 22.06 \pm 0.23$, $i = 20.79 \pm 0.12$, and $z = 20.35 \pm 0.40$, which is located within 0.″4 of the far-infrared position as measured by *Herschel*. The photometric redshift based on the optical magnitudes is $z = 0.69 \pm 0.13$, which is clearly incompatible with the high redshift indicated by the far-infrared photometry and more consistent with the hypothesis that this source is the lensing galaxy (Negrello et al. 2010).

2.1. 30 m Telescope

ID 141 was subsequently observed at the IRAM 30 m telescope on 2010 May 19 using the 117 channel Max-Planck Millimeter Bolometer or MAMBO-2 array to measure the dust continuum flux density at 1.2 mm. The observations were made using the on–off mode, wobbling by 32″ in azimuth at a rate of 2 Hz. The target source was positioned on the most sensitive bolometer, and the correlated sky noise was determined from the other bolometers and subtracted from the "on-source bolometer." The source was observed twice, each time for 10 minutes, yielding a final rms noise level of $\sim$2 mJy. Standard sources (planets and secondary calibration sources) were used for absolute flux calibration. The data were reduced using the standard scripts for on–off observation data in the MOPSIC software package (Zylka 1988). The measured flux density of ID 141 is $S_{1.2\,\mathrm{mJy}} = 36 \pm 2$ mJy, making it one of the high-redshift sources with the largest flux density measured to date at millimeter wavelengths.

Together with the *Herschel* data, the 1.2 mm measurement indicates that the photometric redshift is in the range $3.3 < z_{\mathrm{phot}} < 4.5$—following the method of fitting low-redshift templates to the far-infrared/millimeter available data described in Aretxaga et al. (2005)—a range containing 68% of the probability distribution that corresponds to a very flat distribution due to the lack of photometric data between 500 μm and 1.2 mm, where the peak of the SED is lying.

2.2. Plateau de Bure Interferometer (PdBI)

Based on the redshift range estimated from the available photometric data of *Herschel* and MAMBO, we used the IRAM

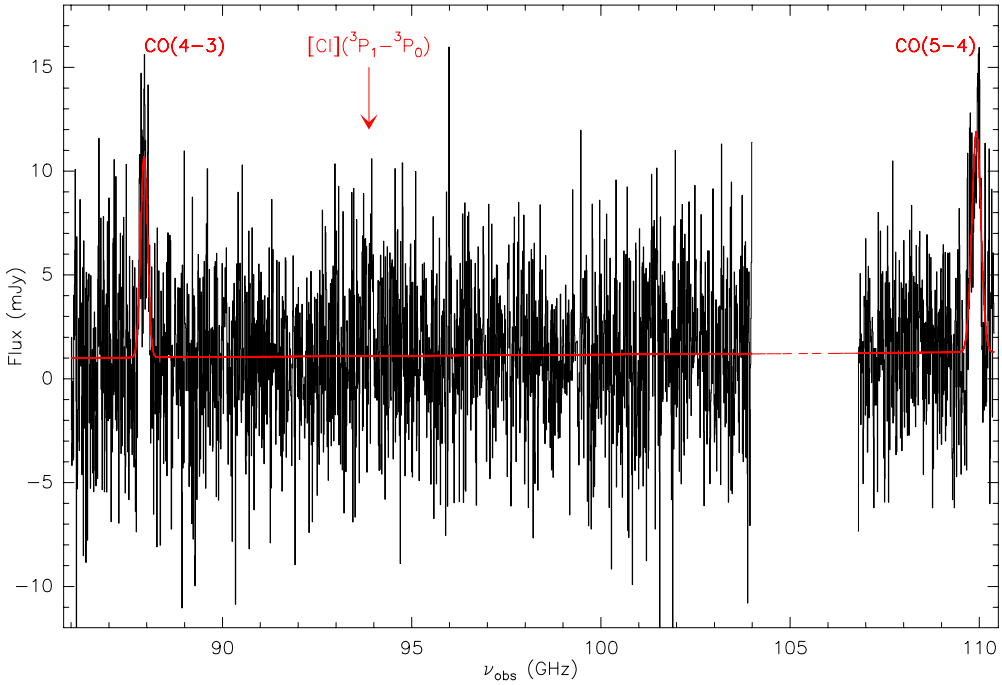

Figure 1. Full frequency sweep done at the PdBI to search for CO emission lines in ID 141, showing the detections of CO($J = 4 \rightarrow 3$) and CO($J = 5 \rightarrow 4$). The $4 \rightarrow 3$ transition was detected first after covering 18 GHz in five frequency setups. The $5 \rightarrow 4$ emission line was detected thereafter in one setting, confirming the redshift of the source at $z = 4.243$. The line shows the continuum at a wavelength of 3 mm that is clearly detected and is increasing from 1.2 ± 0.1 to 1.8 ± 0.3 mJy from the lowest to the highest frequencies—as determined from the averaged line-free channels—see Table 1). The position of the tentatively detected [C I]($^3P_1 - ^3P_0$) emission line is indicated.

Table 2
Parameters of the CO, [C I], and [C II] Emission Lines Observed toward ID 141

Line	ν_{obs} (GHz)	Peak Int. (mJy)	ΔV_{FWHM} (km s^{-1})	I (Jy km s^{-1})	L ($10^9\ L_\odot$)	L' (10^{10} K km s^{-1} pc^2)
CO(4–3)	87.929	9.2 ± 0.7	760 ± 70	7.5 ± 0.9	1.0 ± 0.1	33.4 ± 4.0
CO(5–4)	109.911	13.6 ± 1.1	890 ± 80	13.0 ± 1.6	2.3 ± 0.3	37.1 ± 4.5
CO(7–6)	153.876	7.7 ± 1.2	790 ± 130	6.5 ± 1.4	1.6 ± 0.3	9.4 ± 2.0
[C I]($^3P_1 - ^3P_0$)	93.870	3.0 ± 1.0	790[a]	2.8 ± 0.9	0.42 ± 0.15	10.9 ± 3.5
[C I]($^3P_2 - ^3P_1$)	154.339	4.0 ± 1.0	790 ± 130	3.4 ± 1.1	0.8 ± 0.3	4.9 ± 0.9
[C II]($^2P_{3/2} - ^2P_{1/2}$)	362.45	147 ± 20	690 ± 80	107 ± 17	61.6 ± 9.8	28.1 ± 4.46

Notes. The line luminosities are not corrected for lensing magnification. The amplification factor is supposed to be in the range $10 < \mu_L < 30$—see discussion in Section 3.
[a] Fixed line width.

PdBI (with five antennas) to search for CO emission lines and determine the redshift of ID 141. This search was made possible by the recently installed wideband correlator WideX that provides a continuous frequency coverage of 3.6 GHz bandwidth in dual polarization with a fixed channel spacing of 1.95 MHz. The observations were made in D configuration from 2010 May 23 to May 27 in a series of brief integrations with good atmospheric phase stability (seeing of $1''$) and reasonable transparency (PWV of 5–10 mm). Absolute fluxes were calibrated on MWC 349 when available or on the quasar 1502+1749 whose flux is regularly monitored at the IRAM PdBI. The accuracy of the flux calibration is estimated to be ∼10% at 3 and 2 mm.

We started the line search by tuning the central frequency of the band to 98.6 GHz (96.8–100.4 GHz) with the aim to cover in a series of observations the frequency range from 104.0 to 86.0 GHz that is encompassing the redshift range ($3.5 < z < 4.5$) based on the probability distribution of z_{phot}. For this range in redshift, the expected CO transition is the $4 \rightarrow 3$. For each setting, the rms noise was $1\sigma \sim 4$ mJy in 10 MHz channels after 20 minutes on-source. After five frequency setups, covering 18 GHz from 104 to 86 GHz, a strong and broad emission line was detected at 87.9 GHz with a peak intensity of ∼10 mJy and a zero intensity width of ∼1000 km s^{-1} (Figure 1 and Table 2).

To identify the transition of the CO emission line detected at 87.9 GHz and search for the next higher CO transition, we tuned the receivers to a central frequency of 108.5 GHz covering a redshift range that includes the most probable case where the 87.9 GHz line is the $4 \rightarrow 3$ transition of CO. A strong line was immediately apparent centered at 109.9 GHz, with a peak intensity of ∼13 mJy and a broad-line width comparable to that of the lower frequency line. The two lines at 87.9 and 109.9 GHz are identified with the $4 \rightarrow 3$ and $5 \rightarrow 4$ transitions of CO (Figures 1 and 2). These identifications yield a redshift of $z = 4.243 \pm 0.001$ for ID 141. This is the first "blind" redshift determination using the PdBI.

In addition to the CO emission lines, the 3 mm dust continuum emission was detected at a level of 1.6 ± 0.1 mJy, averaged over the entire line-free range covered at 3 mm, i.e., over ∼19 GHz.

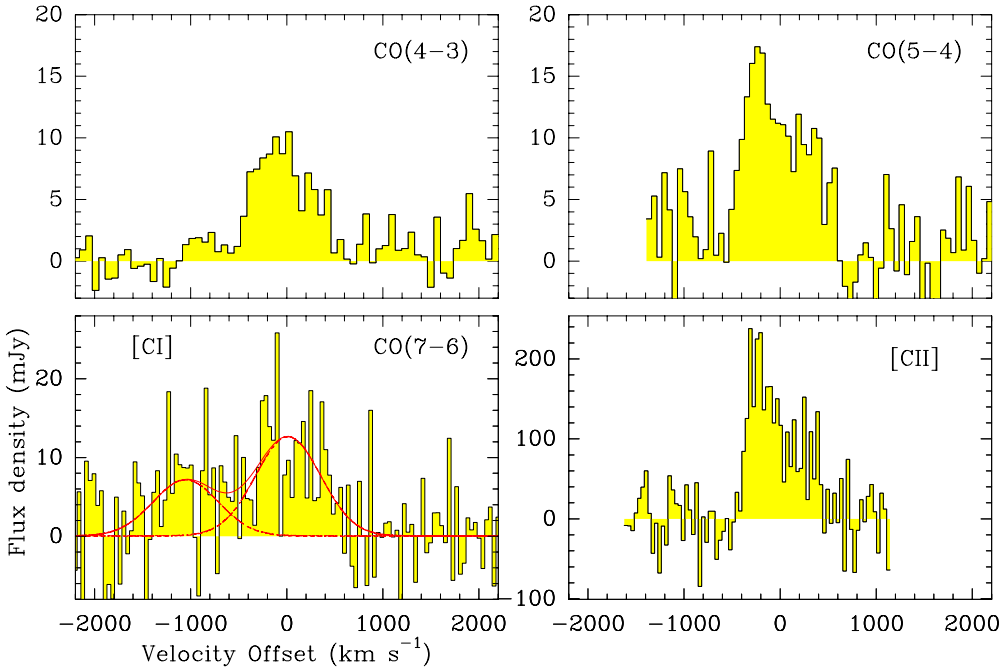

Figure 2. Spectra of the CO($J = 4 \rightarrow 3$) and CO($J = 5 \rightarrow 4$) (upper panels), the CO($J = 7 \rightarrow 6$), [C I]($^3P_2 - ^3P_1$) and [C II]($^2P_{3/2} - ^2P_{1/2}$) emission lines (lower panels) toward ID 141. The continuum was subtracted for all spectra. The velocity scale corresponds to the frequencies ($\nu_{\rm obs}$) listed in Table 2 for the CO and [C II] emission lines (i.e., for the redshift of $z = 4.243$). Gaussian fits to the CO($J = 7 \rightarrow 6$) and [C I] emission lines are shown as dashed curves whereas the full line shows the composite fit.

(A color version of this figure is available in the online journal.)

Table 1 lists the continuum flux densities derived from this 3 mm spectral survey for three different wavelengths (2.75, 3.00, and 3.29 mm) each averaged over ∼4 GHz.

Subsequent observations were performed on 2010 June 29 and September 11, using the compact D configuration under moderate weather conditions (PWV of 5–10 mm, $100 < T_{\rm sys}/{\rm K} < 300$) to search simultaneously for the emission lines of CO($7 \rightarrow 6$) and [C I]($^3P_2 - ^3P_1$) redshifted to 153.876 and 154.339 GHz. Both lines were detected with relatively good signal-to-noise ratio together with the 2 mm dust continuum at a level of 9.7 ± 0.9 mJy (Figure 2). The detection of the [C I]($^3P_2 - ^3P_1$) emission line prompted us to check for the presence of the [C I]($^3P_1 - ^3P_0$) transition that is redshifted to 93.87 GHz and is included in the frequency sweep done from 104.0 to 86.0 GHz. Due to the low signal-to-noise ratio of the sweep, the [C I]($^3P_1 - ^3P_0$) line is detected with a poor signal-to-noise ratio and a line intensity of 2.8 ± 0.9 Jy km s^{-1}.

The parameters of the CO and [C I] lines observed toward ID 141 are listed in Table 2. Figure 3 summarizes the results based on the PdBI observations in a series of maps displaying both the continuum and line emission. The source, which is clearly not multiple, is barely resolved in the PdBI data at the best available beam of $3\farcs6 \times 3\farcs0$ at 2 mm. In the 2 mm continuum map, the integrated flux density of 9.7 ± 0.9 mJy is higher than the emission peak of 5.5 mJy, and a *u–v* fit yields a deconvolved size of $(3.9 \pm 0.4) \times (2.4 \pm 0.4)$ arcsec^2 (or $(27 \times 16)/\mu_{\rm L}$ kpc^2) at an angle of -25 ± 10 deg (NE).

2.3. SMA

ID 141 was observed in the continuum at 880 μm with the Submillimeter Array (SMA) in its compact configuration with eight antennas on 2010 June 15 under moderate weather conditions. The observations on-source amounted to 2.4 hr. The blazar 3C279 was utilized as a bandpass calibrator and Titan as the absolute flux calibrator. The resulting map is shown in Figure 3. The source, which is well detected in the continuum, appears to be relatively small with respect to the PdBI source size and is resolved at the $2''$ resolution. The map rms noise is 1.75 mJy, with a peak of ∼50 mJy. The integrated flux density is 90 ± 2 mJy. To within the limits of the observations, ID 141 appears to be elongated in the northwest direction, in agreement with the 2 mm measurements of the PdBI. The deconvolved size at 0.88 mm is $(2.4 \pm 0.1) \times (1.3 \pm 0.1)$ arcsec^2 (or $(16 \times 9)/\mu_{\rm L}$ kpc^2) at an angle of -32 ± 4 deg (NE). The peak position of ID 141, as derived from the 0.88 mm map, corresponds to R.A. 14:24:13.98 decl. +02:23:03.45 (J2000.0), which is slightly offset by $1\farcs3$ from the position as determined by *Herschel* (see Figure 3). Clearly higher angular resolution observations (both in the sub/millimeter and the optical) are required to further explore the structure of ID 141 and its relation with the lensing galaxy.

2.4. APEX

Observations of the redshifted 1900.538 GHz C[II] line emission in ID 141 were made with the Atacama Pathfinder Experiment (APEX) 12 m telescope in 2010 July in a series of two observing sessions, using the refurbished dual-color FLASH+ MPIfR PI receiver. Its 345 GHz channel now operates wideband IRAM 2SB mixers (Maier et al. 2005). The observations took place on July 7 (where the source was observed for 86 minutes on-time) and July 25 (for 54 minutes on-time) during excellent weather conditions with zenith precipitable water vapor of 0.7 and 0.4 mm. The spectra were taken in a double-beam chopping mode, with a wobbler throw of $50''$ at 1.5 Hz. Pointing was established on nearby Mars and Saturn. At the frequency of 362.45 GHz, the beam size of APEX is $17\farcs8$.

The 4 GHz wide intermediate frequency (IF) of the mixer was connected to a set of fast Fourier transform (FFT)

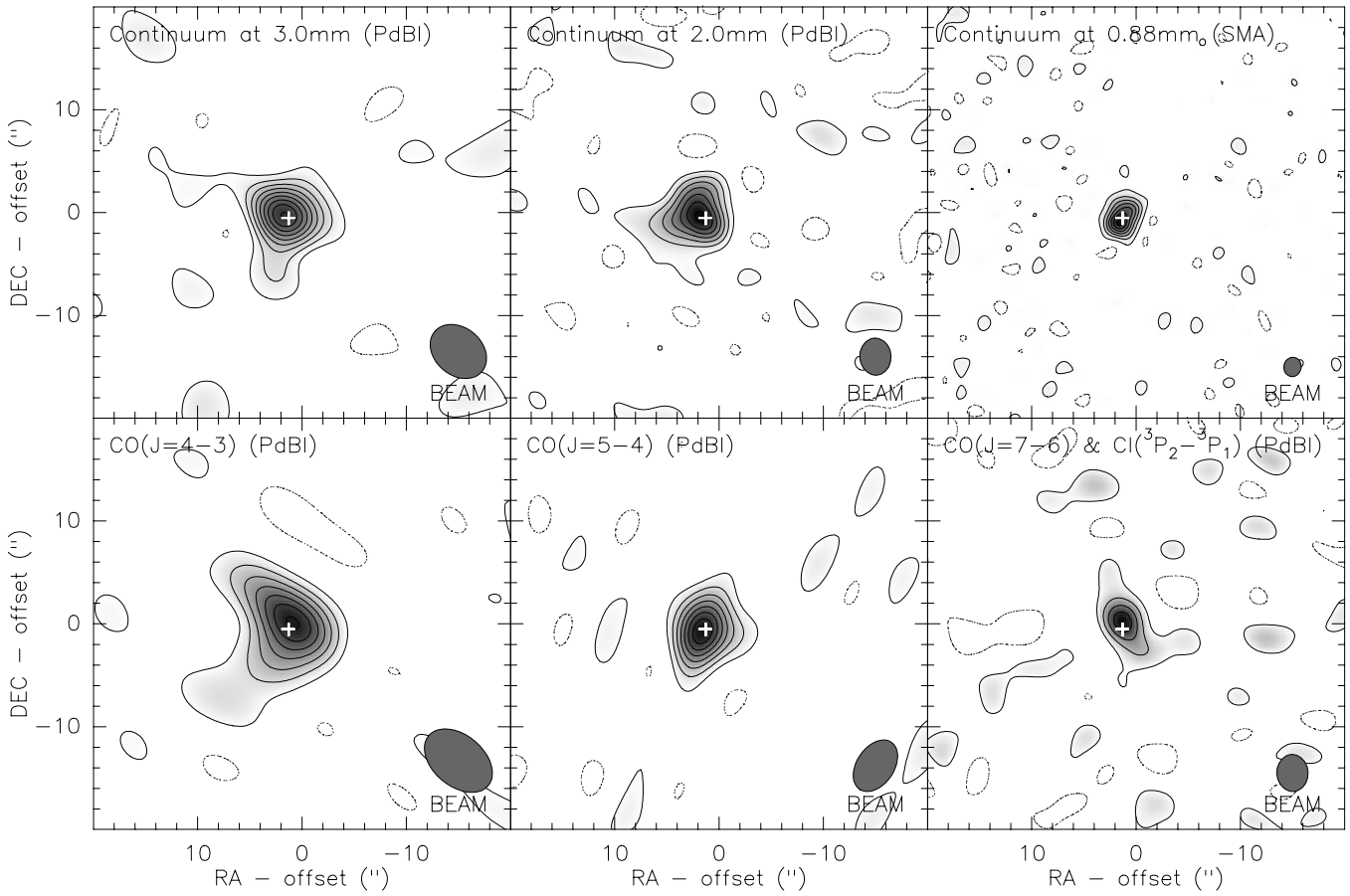

Figure 3. Upper panels: maps of the dust continuum emission at 3, 2, and 0.88 mm toward ID 141. Lower panels: velocity-integrated maps of the three CO and [C I]($^3P_2 - {}^3P_1$) emission lines toward ID 141. All the data were obtained with the PdBI except the 0.88 mm continuum emission that was measured with the SMA. The contours are shown in steps of 2σ, starting at $\pm 2\sigma$, and the synthesized beams are shown in the right lower corner of each panel. The 1σ values are 0.09, 0.3, and 1.75 mJy beam^{-1}, respectively, for the 3, 2, and 0.88 mm continuum maps; 0.56, 0.75, and 1.21 Jy km s^{-1} beam^{-1}, respectively, for the $4 \rightarrow 3$, $5 \rightarrow 4$, and $7 \rightarrow 6$ CO velocity-integrated maps. Offsets are given with respect to the source position as determined by *Herschel* of R.A. 14:24:13.9 decl. +02:23:04 (J2000.0). The white cross indicates the position of the source as determined from the 0.88 mm map and corresponds to R.A. 14:24:13.98 decl. +02:23:03.45 (J2000.0).

spectrometers. In the first observing session, three spectrometers from the CHAMP+FFT backend array, each 1.5 GHz wide, were combined to process, with overlap, a total of 3.4 GHz. In the second run—during their commissioning—two of the new 2.5 GHz wide XFFT spectrometers were connected to cover the full 4 GHz wide IF band (with 500 MHz of overlap), thereby providing 3300 km s^{-1} instantaneous velocity coverage.

The [C II] emission line in ID 141 was readily detected in both observations. For data processing, only linear offsets were removed. The combined spectrum has an rms noise of 1 mK. The line is detected with good signal to noise with a peak flux density of 4 mK in T_a^* and a line shape that is comparable to that of the CO emission lines (Figure 2). The total integrated intensity of the [C II] line is 2.64 ± 0.41 K km s^{-1} or 107 ± 17 Jy km s^{-1} (Table 2)—at 362 GHz, the gain of the APEX is 40.7 Jy K^{-1} in converting T_a^* to flux density (Güsten et al. 2006). Because of the excellent weather conditions, the absolute calibration uncertainties are expected to be of order 10%–20%.

The continuum at 850 μm was measured using the Large APEX Bolometer Camera or LABOCA on 2010 September 20 for a total of about 10 minutes under excellent weather conditions. Planets as well as secondary calibrators were used for absolute flux calibration. The source was detected with a flux density of 102.1 ± 8.8 mJy, in good agreement with the SMA measurements (Table 1). It is noted that the [C II] contribution to the 60 GHz LABOCA passband amounts to only 2.1 mJy or 2%, which is smaller than the uncertainties of the current 850 μm continuum measurement.

3. DISCUSSION

We have detected and/or mapped at high significance three high-J emission lines of CO and the fine-structure emission lines of atomic ([C I]) and singly ionized ([C II]) carbon toward ID 141. Together with the detection and mapping of the far-infrared dust continuum emission, these results are used to constrain the properties of the molecular and atomic gas in this high-redshift galaxy. The detection of the CO emission lines firmly establishes the redshift of ID 141 at $z = 4.243 \pm 0.001$, a value within the redshift range derived from the far-infrared/millimeter photometric measurements. This redshift corresponds to a luminosity distance $D_L = 3.9 \times 10^4$ Mpc and a scale of 6.9 kpc arcsec^{-1}.

3.1. Far-infrared Spectral Energy Distribution

Figure 4 displays the SED of ID 141—based on the flux densities listed in Table 1—where it is compared with the SED of M82. Both SEDs are comparable from the rest-frame submillimeter to far-infrared wavelengths, both peaking at a rest wavelength of $\sim$90 μm. We fit the photometric data points of ID 141 with a single-temperature-modified blackbody spectrum (using the optically thin approximation) by performing a χ^2 fit

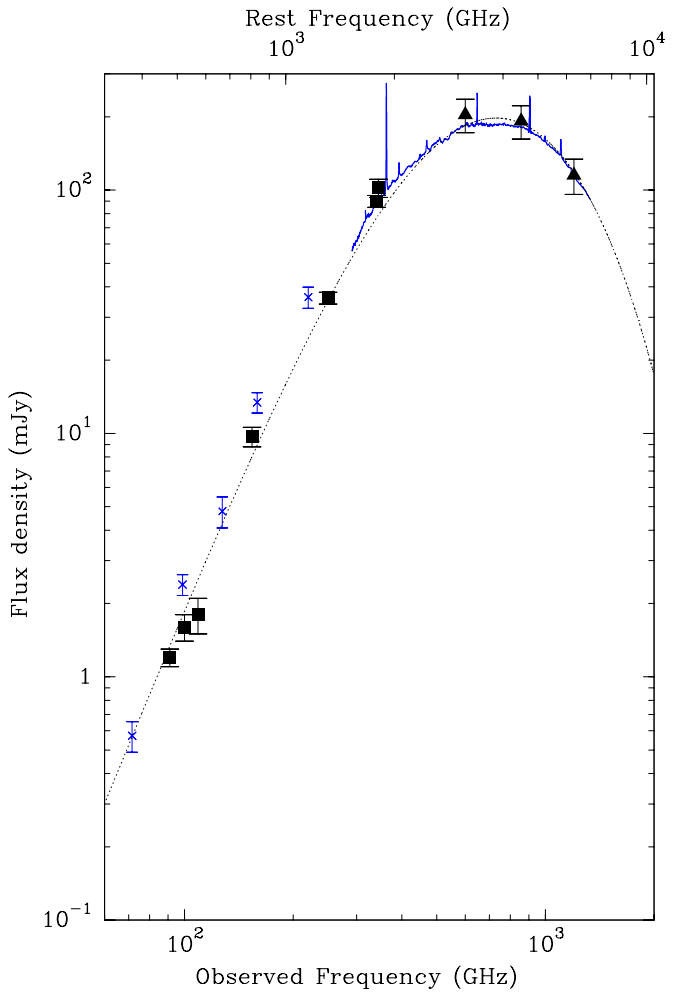

Figure 4. Spectral energy distribution of ID 141 (all measurements from this paper: see Table 1). The squares indicate the ground-based observations and the triangles the *Herschel* SPIRE data. For comparison, the infrared SED of the starburst M82 is displayed, redshifted to $z = 4.24$ and normalized to the flux density of ID 141 at the observed wavelength of 500 μm; the crosses show the photometric data taken from the literature and the continuous line is the *Infrared Space Observatory* Long Wavelength Spectrometer (LWS) spectrum of M82 (Colbert et al. 1999). The dashed line displays the best fit to the photometric data of ID 141 using a single-component, optically thick dust model (as described in the text).

(A color version of this figure is available in the online journal.)

on both the dust temperature ($T_{\rm dust}$) and the dust emissivity index (β) as outlined in Beelen et al. (2006). We derive $\beta = 1.7 \pm 0.1$, $T_{\rm dust} = 38 \pm 1$ K, and a far-infrared luminosity of $L_{\rm FIR} \sim (8.5 \pm 0.3) \times 10^{13}\, \mu_{\rm L}^{-1}\, L_\odot$, where $\mu_{\rm L}$ is the lensing magnification factor. To estimate the dust mass, we adopt for the mass absorption coefficient κ a value of 0.4 cm^2 g^{-1} at 1200 μm (e.g., Beelen et al. 2006). From the above dust temperature and far-infrared luminosity, we derive $M_{\rm dust} \sim 8.9 \times 10^9\, \mu_{\rm L}^{-1}\, M_\odot$. Since the dust emission in luminous infrared starbursts can be optically thick around 100 μm, we also modeled the SED of ID 141 following the analysis described in Weiß et al. (2007). A single-component optically thick dust model (adopting $\beta = 1.7$) fits the photometric data equally well as the optically thin approximation, although with a higher dust temperature ($T_{\rm dust} \approx 58$ K) and a lower dust mass ($M_{\rm dust} \sim 5.5 \times 10^9\, \mu_{\rm L}^{-1}\, M_\odot$). The resulting fit is shown in Figure 4. In this model, the dust becomes opaque ($\tau = 1$) at a rest wavelength of 150 μm (corresponding to an observing frequency of 380 GHz) and the apparent equivalent radius—the true galaxy radius for an unlensed, face-on, filled circular disk (Weiß et al. 2007)—is $r_0 \approx 720\, \mu_{\rm L}^{-1}$ pc.

The global star formation rate (SFR) can be estimated from the far-infrared luminosity using the relation SFR $\approx \delta_{\rm MF}\, (L_{\rm FIR}/10^{10}\, L_\odot)\, M_\odot\, {\rm yr}^{-1}$, where $\delta_{\rm MF}$ is a function of the present mass composition of the stellar population (Omont et al. 2001). For a range of metallicities, initial mass functions, and starburst ages of 10–100 Myr, $\delta_{\rm MF}$ ranges in between 0.8 and 2. Under the assumption that the far-infrared luminosity of ID 141 is dominated by starburst activity, we estimate that $0.7 \times 10^4\, \mu_{\rm L}^{-1}\, M_\odot\, {\rm yr}^{-1} < {\rm SFR} < 1.7 \times 10^4\, \mu_{\rm L}^{-1}\, M_\odot\, {\rm yr}^{-1}$, which is an upper limit in case there is an Active Galactic Nucleus (AGN) contribution to the far-infrared luminosity.

Using the Faint Images of the Radio Sky at twenty-one centimeters (FIRST) survey (Becker et al. 1995), the 1.4 GHz flux density of ID 141 is measured to be $S_{1.4\,\rm GHz} = 570 \pm 160\, \mu$Jy, which shows that ID 141 is not a radio-loud source. For ID 141, the far-infrared/radio parameter $q = \log_{10}[(F_{\rm IR}/3.75 \times 10^{12}\, {\rm W\, m^{-2}})/(S_{1.4\rm GHz}/{\rm W\, m^{-2}\, Hz^{-1}})]$ (Condon 1992) is estimated to be $q \sim 2.1 \pm 0.1$, after K-correcting and assuming a canonical radio slope for a star-forming galaxy $\alpha = -0.75$, where $S_\nu \propto \nu^\alpha$. This value is compatible with the median value $q \sim 2.4$ derived for starburst samples selected from the Balloon-borne Large-Aperture Telescope (BLAST) or the *Herschel* GOODS-North surveys (Ivison et al. 2010a, 2010b; Jarvis et al. 2010). This suggests that star formation activity is responsible for most of the far-infrared luminosity of ID 141.

Typical amplification factors of 10–30 have been estimated for sources similar to ID 141 with 500 μm flux density above 100 mJy uncovered in the H-ATLAS survey (Negrello et al. 2010). We therefore adopt in this paper a magnification range of $10 < \mu_{\rm L} < 30$ for ID 141. Under this assumption, the far-infrared luminosity, dust mass, and global star formation of ID 141 are estimated to be in the range: (2.8–8.5) $\times 10^{12}\, L_\odot$ for $L_{\rm FIR}$, (3–9) $\times 10^8\, M_\odot$ for $M_{\rm dust}$, and (200–1700) $M_\odot\, {\rm yr}^{-1}$ for SFR. These values are typical for the population of dusty, gas-rich, and luminous SMGs found at high redshift (Greve et al. 2005; Tacconi et al. 2010).

3.2. The CO Emission Lines

The CO lines of ID 141 are broad ($\Delta V_{\rm FWHM} \sim 800\, {\rm km\, s^{-1}}$—see Table 2) and display a clear, asymmetrical, and double-peaked profile where the blue part of the line is stronger than its red counterpart (Figure 2). A similar profile is seen in the [C II] emission line. The blue and redshifted peaks of the lines are found from Gaussian fits at velocity offsets of $\pm 220\, {\rm km\, s^{-1}}$, respectively, each with an FWHM of $\sim 400\, {\rm km\, s^{-1}}$. The broad-line width of ID 141 compares with the median FWHM ($780 \pm 320\, {\rm km\, s^{-1}}$) of high-redshift SMGs, and double-peaked asymmetrical line shapes have also been reported for other luminous SMGs (Greve et al. 2005; Swinbank et al. 2010). Such double-peaked line profiles indicate orbital motions under the influence of gravity either in the form of a disk or a merger. However, the current angular resolution of the observations presented in this paper does not allow us to distinguish between the two scenarios and attempts to find positional offsets between the blue and redshifted peaks remained inconclusive. Higher resolution observations in either CO or [C II] are required to further examine the structure of the velocity gradient in ID 141.

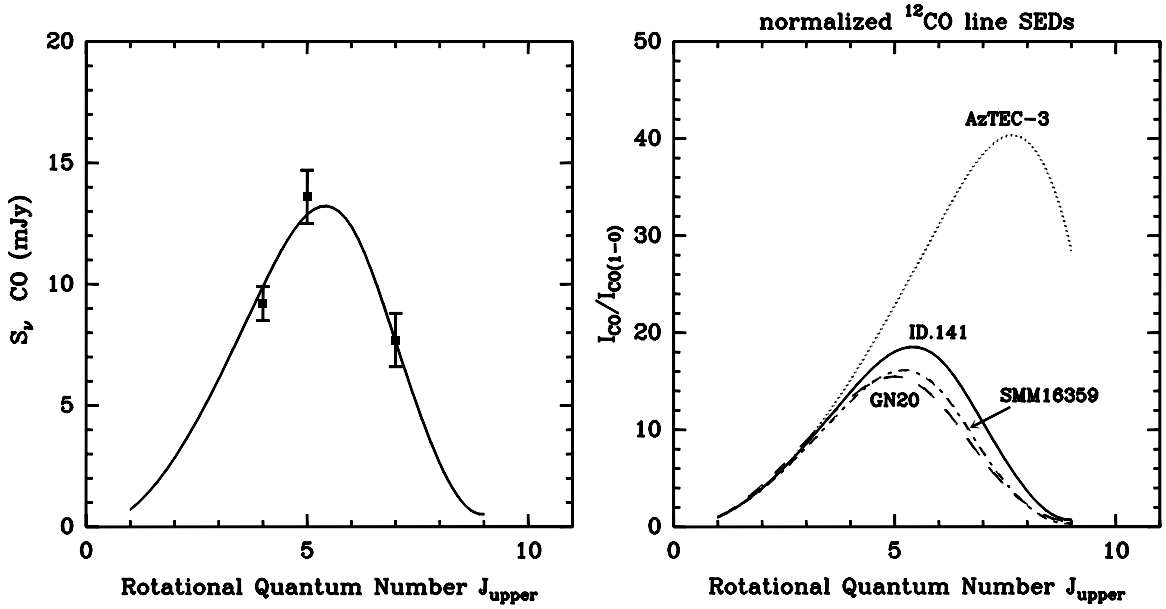

Figure 5. Left panel: observed CO fluxes vs. rotational quantum number (CO line SED) for ID 141. The single-component LVG model (described in the text) corresponds to $n(H_2) = 10^{3.9}$ cm^{-3} and $T_{kin} = 40$ K. Right panel: comparison of the CO line SEDs of ID 141 and selected high-z SMGs: GN20 ($z = 4.05$) (Carilli et al. 2010), SMM16359 ($z = 2.5$) (Weiß et al. 2005b), and AzTEC-3 ($z = 5.3$) (Riechers et al. 2010). The CO line SEDs are normalized by their CO(1–0) flux density.

From the line parameters listed in Table 2 and following the definition for line luminosity given by Equation (3) in Solomon et al. (1997), the CO line luminosities are $L' = (3.34 \pm 0.40)$, (3.71 ± 0.45), and $(0.94 \pm 0.20) \times 10^{11}\,\mu_L^{-1}$ K km s^{-1} pc^2 for the $4 \rightarrow 3$, $5 \rightarrow 4$, and $7 \rightarrow 6$ transitions, respectively. This corresponds to CO($J = 5 \rightarrow 4$)/CO($J = 4 \rightarrow 3$) and CO($J = 7 \rightarrow 6$)/CO($J = 5 \rightarrow 4$) line brightness temperature ratios of $r_{54} = 1.1 \pm 0.1$ and $r_{75} = 0.24 \pm 0.04$, indicating that the higher CO transitions are not thermalized (see also values of L'_{CO} in Table 2).

To describe the properties of the molecular gas in more detail, we have analyzed the CO data using a spherical, single-component, large velocity gradient (LVG) model (Weiß et al. 2007). As in Weiß et al. (2007), we adopt a CO abundance per velocity gradient of $[CO]/(dv/dr) = 10^{-5}$ pc (km s^{-1})$^{-1}$ that best fits the high-J lines and implies low enough opacities to reproduce the fluxes of the two lower CO transitions. The results of the best-fit model, which are displayed in Figure 5, correspond to an H_2 density of $n_{H_2} = 10^{3.9}$ cm^{-3}, a gas temperature of $T_{kin} = 40$ K, and an equivalent (magnified) radius of $r_0 = 680$ pc. These values are comparable to those derived for other high-redshift SMGs such as GN20 at $z = 4.04$ (Carilli et al. 2010) and SMM16359 at $z = 2.5$ (Weiß et al. 2005b), as shown in Figure 5. Typical degeneracies between the temperature and density in such LVG models are discussed in Weiß et al. (2007). Additional CO transitions, in particular the low-J transitions, should be observed to evaluate more precisely the density and the temperature of the molecular gas and check whether an excess of cold molecular gas could be present (Ivison et al. 2011). Based on this model, the expected CO(1–0) line luminosity is $L'_{CO(1-0)} = 4.3 \times 10^{11}\,\mu_L^{-1}$ K km s^{-1} pc^2 or $L_{CO(1-0)} = 2.1 \times 10^7\,\mu_L\,L_\odot$. Assuming a conversion factor of $\alpha_{CO} = 0.8\,M_\odot$ (K km s^{-1} pc^2)$^{-1}$ from $L'_{CO(1-0)}$ to M_{H_2}, appropriate for starburst galaxies as derived from observations of local ULIRGs (Downes & Solomon 1998; Tacconi et al. 2008), yields a molecular gas mass $M_{H_2} = 3.5 \times 10^{11}\,\mu_L^{-1}\,M_\odot$. After correction for the amplification, the above values are comparable to the median gas mass ($3 \times 10^{10}\,M_\odot$) derived for luminous SMGs using the same conversion factor α_{CO} (Greve et al. 2005) and the gas masses of (1–3) $\times 10^{10}\,M_\odot$ measured in the H-ATLAS high-redshift-lensed SMGs SPD 81 and SPD 130 discovered by the *Herschel Space Observatory* (Frayer et al. 2010).

3.3. The Carbon Fine-structure Atomic Lines

3.3.1. The [C II] Emission Line

From the total integrated intensity, the [C II] line luminosity for ID 141 is $L_{C\,II} = (6.1 \pm 0.9) \times 10^{10}\,\mu_L^{-1}\,L_\odot$. Correcting for the amplification factor, the value of $L_{C\,II}$ for ID 141 is therefore comparable to that of other high-redshift sources, such as: SDSS J1148+5251 ($z = 6.42$) with $(4.4 \pm 0.5) \times 10^9\,L_\odot$ (Maiolino et al. 2005; Walter et al. 2009), BR 0952−0115 ($z = 4.43$) with $(4.6 \pm 0.7) \times 10^9\,L_\odot$ (Maiolino et al. 2009), BRI 1335−0417 ($z = 4.40$) with $(16.4 \pm 2.6) \times 10^9\,L_\odot$ (Wagg et al. 2010), SMM J2135−0102 (the "Eyelash" at $z = 2.3$) with $(5.5 \pm 1.3) \times 10^9\,L_\odot$ (Ivison et al. 2010c), or the SMG LESS J033229.4 ($z = 4.76$) with $(1.02 \pm 0.15) \times 10^{10}\,L_\odot$ (De Breuck et al. 2011). The [C II] line luminosities for these high-redshift infrared luminous galaxies are, however, lower than most of the values derived for a sample of 14 galaxies at redshifts $1 < z < 2$ that have bright [C II] emission lines yielding luminosities in the range $8 \times 10^9 < L_{C\,II}/L_\odot < 10^{11}$ (Hailey-Dunsheath et al. 2010; Stacey et al. 2010).

For ID 141, we derive a ratio $L_{[C\,II]}/L_{FIR} = (7.3 \pm 1.31) \times 10^{-4}$. This is higher than for most of the high-redshift sources with similar infrared luminosity and redshift but comparable to BRI 1335−0417 where the ratio is $(5.3 \pm 0.8) \times 10^{-4}$ (Wagg et al. 2010). ID 141 follows the trend reported for high-z luminous galaxies in the relation of $L_{[C\,II]}/L_{FIR}$ as a function of the far-infrared luminosity L_{FIR}, with a ratio of about one order of magnitude lower than for normal galaxies but comparable to ULIRG values (Figure 6).

Recently, Graciá-Carpio et al. (2011) showed that the ratio between the far-infrared luminosity and the molecular gas mass, L_{FIR}/M_{H_2}, appears to be a better choice from a physical

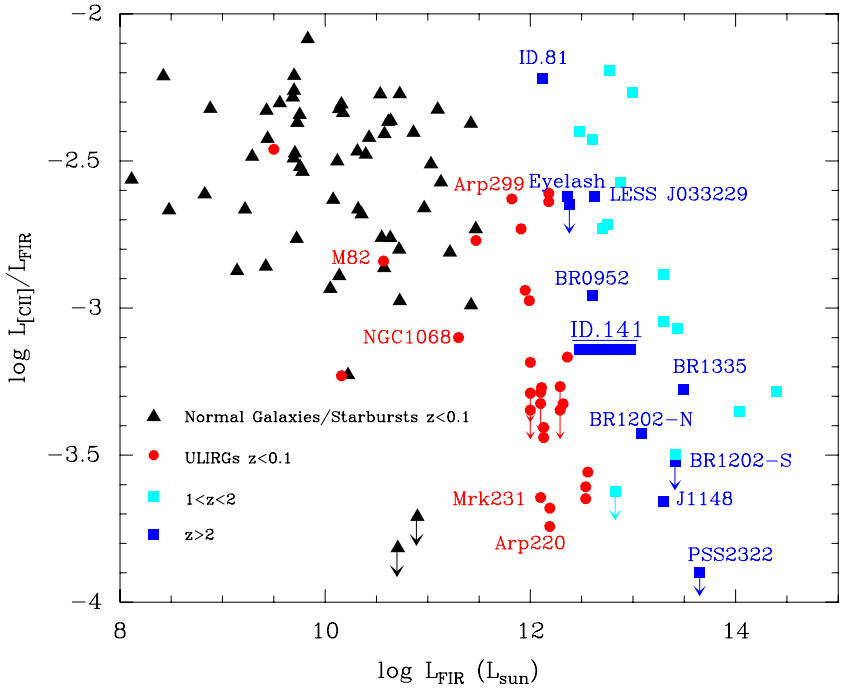

Figure 6. $L_{\rm C\,II}/L_{\rm FIR}$ as a function of the far-infrared luminosity for normal galaxies (Malhotra et al. 2001; Colbert et al. 1999; Unger et al. 2000; Spinoglio et al. 2005; Carral et al. 1994) and ULIRGs (Luhman et al. 1998, 2003) in the local universe, and starburst galaxies and AGNs at $1 < z < 2$ (Stacey et al. 2010) and $z > 3$—see the text for references. The source ID 141 is labeled (an underlined) as well as other well-known local starbursts (including M82) and high-redshift sources. The source ID 81 ($z = 3.04$) is a recent measurement based on SPIRE Fourier Transform Spectrometer (FTS) observations (Valtchanov et al. 2011). For ID 141, the bar shows the range in far-infrared luminosity after correcting for an amplification factor $10 < \mu_{\rm L} < 30$.

point of view to investigate the relative brightness of the far-infrared fine-structure lines in galaxies. This ratio, which removes the uncertainty of the amplification factor, also appears to better reflect the properties of the gas than $L_{\rm FIR}$ alone. Graciá-Carpio et al. (2011) found that there is a threshold at $L_{\rm FIR}/M_{\rm H_2} \sim 80\,L_\odot\,M_\odot^{-1}$ above which galaxies tend to have weaker [C II] emission with respect to their far-infrared luminosity. This threshold is similar to the one separating the star formation relations between non- or weakly-interacting star-forming galaxies and luminous mergers (Genzel et al. 2010, Daddi et al. 2010). With a ratio $L_{\rm FIR}/M_{\rm H_2} \sim 230\,L_\odot\,M_\odot^{-1}$, ID 141 follows the trend in the $L_{\rm [C\,II]}/L_{\rm FIR}$ versus $L_{\rm FIR}/M_{\rm H_2}$ plane reported in Graciá-Carpio et al. (2011), indicating that its ionization parameter must be high ($\sim 10^{-2}$) and that ID 141 could be a luminous merger.

Another sensitive probe of the physical conditions within the interstellar medium is the ratio $L_{\rm C\,II}/L_{\rm CO(1-0)}$. For ID 141, we find $L_{\rm C\,II}/L_{\rm CO(1-0)} \sim 2900$ from the measured [C II] and the estimated CO(1–0) luminosities. Using the photon-dominated region (PDR) model and diagnostic diagram comparing the ratios $L_{\rm C\,II}/L_{\rm FIR}$ versus $L_{\rm CO(1\to0)}/L_{\rm FIR}$ (Kaufman et al. 1999) indicates that, for ID 141, the gas is dense with $n \sim 10^4$ cm^{-3} and that the far-UV radiation field illuminating the PDR, G_0, is a few 10^3 times more intense than that in our Galaxy. Both these values point to physical conditions comparable to those found in the central regions of local ULIRGs (Stacey et al. 2010).

3.3.2. The [C I] Emission Line

The [C I]($^3P_2 - {}^3P_1$) line flux implies $L_{\rm C\,I} = (0.8 \pm 0.3) \times 10^9\,\mu_{\rm L}^{-1}\,L_\odot$ (Table 2). The [C I] luminosity in ID 141, once corrected for the amplification, is therefore lower than the [C I] luminosities derived from the ($^3P_2 - {}^3P_1$) transition for other high-redshift sources such as the Cloverleaf (Weiß et al. 2003, 2005a) or PSS 2322+1944 (Pety et al. 2004) or other high-redshift galaxies or quasars (Walter et al. 2011). Assuming an excitation temperature ($T_{\rm ex}$) equal to the temperature of the dust and gas, i.e., $T_{\rm ex} \sim 40$ K, the mass of neutral carbon in ID 141 amounts to $M_{\rm C\,I} = (6.5 \pm 1.1) \times 10^7\,\mu_{\rm L}^{-1}\,M_\odot$, a result that is only weakly dependent on $T_{\rm ex}$ (Pety et al. 2004). Compared to the mass of molecular gas, the derived mass of [C I] implies a neutral carbon abundance relative to H_2 of $[{\rm C\,I}]/[{\rm H_2}] \approx 1.8 \times 10^{-5}$. The similarity of this abundance to the value of 2.2×10^{-5} found for Galactic dense molecular clouds (Frerking et al. 1989) is indicative of a substantial enrichment in ID 141. In addition, the $L_{\rm C\,I(1-0)}/L_{\rm FIR}$ luminosity ratio is also a sensitive measurement of G_0 (Kaufman et al. 1999; Gérin & Phillips 2000). For ID 141, $L_{\rm C\,I(1-0)}/L_{\rm FIR} \approx 5 \times 10^{-6}$ close to the luminosity ratio found in other high-z sources (Walter et al. 2011) and indicating a high UV field strength of $G_0 \sim 3 \times 10^3$, compatible with the analysis based on the [C II] emission line.

The measurements available for ID 141 allow an estimate of the relative cooling of the carbon and CO emission lines. The upper transition of [C I] is stronger than the lower transition by a factor of $\approx$2 (Table 2), as in the case of the Cloverleaf (Weiß et al. 2005a). The total luminosity of ID 141 in [C I] is therefore $\approx 1.2 \times 10^9\,\mu_{\rm L}^{-1}\,L_\odot$. Based on the LVG model described above, the total CO line luminosity in ID 141 is estimated to be $L_{\rm CO} \approx 8.4 \times 10^9\,\mu_{\rm L}^{-1}\,L_\odot$. The CO/[C I] luminosity ratio is thus $\approx$7.0 and the cooling in the CO and [C I] lines represents 10^{-4} of the far-infrared continuum, a factor of seven lower than the main cooling line of the gas, i.e., the [C II] transition.

4. CONCLUSIONS

We have used four ground-based (sub)millimeter facilities—the IRAM 30 m and PdBI, the SMA, and APEX—to follow up the exceptional source ID 141, the strongest 500 μm

peaker yet discovered in the *Herschel* cosmological surveys. The detection of three bright CO emission lines using the PdBI confirms that the source is at high redshift ($z = 4.243$). The strength of the continuum and the intensities of the molecular and atomic emission lines of ID 141 suggest that the source is gravitationally lensed, in line with what was already found for other submillimeter-bright, high-redshift, galaxies detected with the *Herschel Space Observatory* (Negrello et al. 2007, 2010). The magnification factor is still unknown but is likely to be in the range of $10 < \mu_{\rm L} < 30$ as found for other gravitationally lensed SMGs uncovered in the H-ATLAS survey. The properties of the molecular and atomic gas in ID 141 indicate properties of a luminous ($L_{\rm FIR} \sim (3\text{–}8) \times 10^{12}\,L_{\odot}$), dense ($n \approx 10^4\,{\rm cm}^{-3}$), and warm ($T_{\rm kin} \approx 40\,{\rm K}$) starburst galaxy that are comparable to those derived for local starburst galaxies or high-redshift SMGs. The asymmetric double profiles of the carbon and CO emission lines are indicative of orbital motions in a disk or a merger. The source is barely resolved in the present data, indicating a physical size that is smaller than $14/\mu_{\rm L}$ kpc, corresponding to an upper limit of $2''$.

The measurements of the carbon lines ([C I] and [C II]) enable a first study of the gas associated with the PDR in ID 141 and analysis of the relative cooling of the carbon and CO emission in this galaxy, that is dominated by that of C^+. The [C II]-to-FIR luminosity ratio, $(7.3 \pm 1.3) \times 10^{-4}$, is larger than the one found for other high-redshift galaxies of comparable luminosity and redshift, and consistent with recent findings that the scatter in the $L_{\rm C\,II}/L_{\rm FIR}$ versus $L_{\rm FIR}$ diagram is indeed large. With a ratio of $L_{\rm FIR}/M_{\rm H_2} \sim 230\,L_{\odot}\,M_{\odot}^{-1}$, ID 141 follows the trend reported by Graciá-Carpio et al. (2011) in the $L_{\rm C\,II}/L_{\rm FIR}$ versus $L_{\rm FIR}/M_{\rm H_2}$ plane, suggesting both a high-ionization parameter and the fact that ID 141 could be a merger.

The present observations underline the importance of observations done at frequencies in between 85 and 360 GHz to study the properties of galaxies at redshift $z > 4$. In particular, the lower frequencies (in the 3 and 2 mm windows) are essential to probe the peak of the CO emission that, for such starburst galaxies, lies around $J_{\rm upper}$ 4–5, as well as the two emission lines of [C I] or molecules other than CO such as water. Follow-up observations of very high-redshift, obscured galaxies found in future deep surveys, especially the less luminous objects, will need sensitive interferometers operating at frequencies below 350 GHz, such as the Atacama Large Millimeter Array (ALMA), the Expanded Very Large Array (EVLA), or the future upgrade of the PdBI (the Northern Extended Millimeter Array or NOEMA) in order to fully explore the properties of the molecular and atomic gas in starburst galaxies that were active when the universe was about 1 Gyr old.

The results described in this paper are based on observations obtained with *Herschel*, an ESA space observatory with science instruments provided by European-led Principal Investigator consortia and with important participation from NASA. US participants in H-ATLAS acknowledge support from NASA through a contract from JPL. The ground-based follow-up observations were obtained at the following facilities. The 30 m telescope and the PdBI of IRAM that is funded by the Centre National de la Recherche Scientifique (France), the Max-Planck Gesellschaft (Germany), and the Instituto Geografico Nacional (Spain). APEX is a collaboration between the Max-Planck-Institut für Radioastronomie, the European Southern Observatory, and the Onsala Space Observatory. The Submillimeter Array (SMA) is a joint project between the Smithsonian Astrophysical Observatory and the Academia Sinica Institute of Astronomy and Astrophysics and is funded by the Smithsonian Institution and the Academia Sinica. Part of this study was supported by financial contribution from the agreement ASI-INAF I009/10/0 and by CONACyT grant 39953-F.

Facilities: *Herschel* (SPIRE), IRAM:30m, IRAM: Interferometer, SMA, APEX

REFERENCES

Aretxaga, I., Hughes, D. H., & Dunlop, J. S. 2005, MNRAS, 358, 1240
Becker, R. H., White, R. L., & Helfand, D. J. 1995, ApJ, 450, 559
Beelen, A., Cox, P., Benford, D., et al. 2006, ApJ, 642, 694
Blain, A. W. 1996, MNRAS, 283, 1340
Blain, A. W., Kneib, J.-P., Ivison, R. J., & Smail, I. 1999, ApJ, 512, L87
Blain, A. W., Smail, I., Ivison, R. J., Kneib, J.-P., & Frayer, D. T. 2002, Phys. Rep., 369, 111
Carilli, C. L., Daddi, E., Riechers, D., et al. 2010, ApJ, 714, 1407
Carral, P., Hollebach, D. J., Lord, S. D., et al. 1994, ApJ, 423, 223
Colbert, J. W., Malkan, M. A., Clegg, P. E., et al. 1999, ApJ, 511, 721
Condon, J. J. 1992, ARA&A, 30, 572
Conley, A., Cooray, A., Vieira, J. D., et al. 2011, ApJ, 732, L35
Daddi, E., Elbaz, D., Walter, F., et al. 2010, ApJ, 714, L118
Danielson, A. L. R., Swinbank, A. M., Smail, I., et al. 2011, MNRAS, 410, 1687
De Breuck, C., Maiolino, R., Caselli, P., et al. 2011, A&A, 530, L8
Downes, D., & Solomon, P. M. 1998, ApJ, 507, 615
Downes, D., Solomon, P. M., & Radford, S. J. E. 1995, ApJ, 453, L65
Eales, S., Dunne, L., Clements, D., et al. 2010, PASP, 122, 499
Frayer, D. T., Harris, A. I., Baker, A. J., et al. 2010, ApJ, 726, L22
Frerking, M. A., Keene, J., Blake, G. A., & Phillips, T. G. 1989, ApJ, 344, 311
Genzel, R., Tacconi, L. J., Graciá-Carpio, J., et al. 2010, MNRAS, 407, 2091
Gérin, M., & Phillips, T. G. 2000, ApJ, 537, 644
Graciá-Carpio, J., Sturm, E., Hailey-Dunsheath, S., et al. 2011, ApJ, 728, L7
Greve, T. R., Bertoldi, F., Smail, I., et al. 2005, MNRAS, 359, 1165
Griffin, M. J., Abergel, A., Abreu, A., et al. 2010, A&A, 518, L3
Güsten, R., Nyman, L. A., Schilke, P., et al. 2006, A&A, 454, L13
Hailey-Dunsheath, S., Nikola, T., Stacey, G. J., et al. 2010, ApJ, 714, L162
Hopwood, R., Serjeant, S., Negrello, M., et al. 2010, ApJ, 716, L45
Hughes, D. H., Serjeant, S., Dunlop, J., et al. 1998, Nature, 394, 241
Ivison, R. J., Alexander, D. M., Biggs, A. D., et al. 2010a, MNRAS, 402, 245
Ivison, R. J., Magnelli, B., Ibar, E., et al. 2010b, A&A, 518, L31
Ivison, R. J., Papadopoulos, P. P., Smail, I., et al. 2011, MNRAS, 411, 1913
Ivison, R. J., Swinbank, A. M., Swinyard, B., et al. 2010c, A&A, 518, L35
Jarvis, M., Smith, D. J. B., Bonfield, D. G., et al. 2010, MNRAS, 409, 92
Kaufman, M. J., Wolfire, M. G., Hollenbach, D. J., & Luhman, M. L. 1999, ApJ, 527, 795
Luhman, M. L., Satyapal, S., Fischer, J., et al. 1998, ApJ, 504, L11
Luhman, M. L., Satyapal, S., Fischer, J., et al. 2003, ApJ, 594, 758
Magnelli, B., Elbaz, D., Chary, R. R., et al. 2009, A&A, 496, 57
Maier, D., Barbier, A., Lazareff, B., & Schuster, K.-F. 2005, in 16th Int. Symp. on Space Terahertz Technology, 2005 May 2–4, Chalmers University of Technology, Göteborg, Sweden, 428
Maiolino, R., Caselli, P., Nagao, T., et al. 2009, A&A, 500, L1
Maiolino, R., Cox, P., Caselli, P., et al. 2005, A&A, 440, L51
Malhotra, S., Kaufman, M. J., Hollenbach, D., et al. 2001, ApJ, 561, 766
Negrello, M., Hopwood, R., De Zotti, G., et al. 2010, Science, 330, 800
Negrello, M., Perrotta, F., González-Nuevo, J., et al. 2007, MNRAS, 377, 1557
Omont, A., Cox, P., Bertoldi, F., et al. 2001, A&A, 374, 371
Pety, J., Beelen, A., Cox, P., et al. 2004, A&A, 428, L21
Pilbratt, G. L., Riedinger, J. R., Passvogel, T., et al. 2010, A&A, 518, L1
Poglitsch, A., Waelkens, C., Geis, N., et al. 2010, A&A, 518, L2
Riechers, D. A., Capak, P. L., Carilli, C. L., et al. 2010, ApJ, 720, L131
Rowan-Robinson, M., Broadhurst, T., Oliver, S. J., et al. 1991, Nature, 351, 719
Smail, I., Ivison, R. J., & Blain, A. W. 1997, ApJ, 490, L5
Solomon, P. M., Downes, D., Radford, S. J. E., & Barrett, J. W. 1997, ApJ, 478, 144
Spergel, D. N., Verde, L., Peiris, H. V., et al. 2003, ApJS, 148, 175
Spinoglio, L., Malkan, M. A., Smith, H., González-Alfonso, E., & Fischer, J. 2005, ApJ, 623, 123
Stacey, G. J., Hailey-Dunsheath, S., Ferkinhoff, C., et al. 2010, ApJ, 724, 957
Swinbank, A. M., Smail, I., Longmore, S., et al. 2010, Nature, 464, 733
Tacconi, L. J., Genzel, R., Neri, R., et al. 2010, Nature, 463, 781
Tacconi, L. J., Genzel, R., Smail, I., et al. 2008, ApJ, 680, 246

Unger, S. J., Clegg, P. E., Stacey, G. J., et al. 2000, A&A, 355, 885
Valtchanov, I., Virdee, J., Ivison, R.J., et al. 2011, MNRAS, 415, 3473
Vieira, J. D., Crawford, T. M., Switzer, E. R., et al. 2010, ApJ, 719, 763
Wagg, J., Carilli, C. L., Wilner, D. J., et al. 2010, A&A, 519, L1
Walter, F., Riechers, D., Cox, P., et al. 2009, Nature, 457, 699
Walter, F., Weiß, A., Downes, D., Decarli, R., & Henkel, C. 2011, ApJ, 730, 18
Weiß, A., Downes, D., Henkel, C., & Walter, F. 2005a, A&A, 429, L25
Weiß, A., Downes, D., Neri, R., et al. 2007, A&A, 467, 955
Weiß, A., Downes, D., Walter, F., & Henkel, C. 2005b, A&A, 440, L45
Weiß, A., Henkel, C., Downes, D., & Walter, F. 2003, A&A, 409, L41
York, D. G., Adelman, J., Anderson, J. E., Jr., et al. 2000, AJ, 120, 1579
Zylka, R. 1988, MPOSI Users Manual (Grenoble: IRAM)